J. Fluid Mech. (2006), *vol.* 553, *pp.* 85–105. © 2006 Cambridge University Press
doi:10.1017/S0022112006008706 Printed in the United Kingdom

On viscous beads flowing down a vertical fibre

By R. V. CRASTER[1] AND O. K. MATAR[2]

[1]Department of Mathematics, Imperial College London, SW7 2AZ, UK
[2]Department of Chemical Engineering, Imperial College London, SW7 2AZ, UK

(Received 12 April 2005 and in revised form 11 October 2005)

The vertical flow of a fluid, under the influence of gravity, down the exterior of a rigid fibre is a flow accompanied by rich dynamics manifested via the formation of droplets, or beads, driven by a Rayleigh mechanism modulated by the presence of gravity. These droplets propagate down the fibre and undergo coalescence with preceding droplets. Different flow regimes are possible depending on system parameters such as the fibre radius, liquid flow rate and physical properties. We derive an evolution equation for the interface in the long-wavelength approximation, which captures the flow characteristics of the system; this model is similar to those previously used to investigate the dynamics of slender viscous threads in the absence of the fibre. Analytical and numerical solutions of the evolution equation yield information regarding the shape and propagation speeds of the droplets, which is in good agreement with available experimental data as well as those obtained as part of the present work. Connections with models already available in the literature are also established.

1. Introduction

Cylindrical fluid threads and jets have been much studied since the seminal work of Lord Rayleigh (1878) who identified the mechanism by which droplets form under the action of surface tension. The dynamics and scalings of the breakup of fluid jets and threads is of recurrent interest; a review of the recent literature is provided by Eggers (1997). A related flow is that of a fluid film flowing on a circular fibre under the influence of gravity. Here, surface tension is destabilizing leading to the formation of droplets or beads on the fibre. This flow is the subject of the present work.

The coating of fibres has received some attention in the literature, mainly in connection with the drawing of fibres from baths containing liquids in the presence or absence of surfactant (Quéré 1999; Shen *et al.* 2002). The vertical flow down the fibre has also been studied by several authors: experimental studies have shown that the presence of a mean flow field modulates the surface-tension-driven flow, which can potentially lead to film breakup, giving rise to interfacial waves of finite amplitude (Quéré 1990; De Ryck & Quéré 1996). Most of the modelling work in this area has mainly focused on the use of a lubrication-type approximation wherein the fibre radius is taken to be much larger than the film thickness (see, for instance, Frenkel 1992; Kalliadasis & Chang 1994; Kerchman & Frenkel 1994; Chang & Demekhin 1999; Roy, Roberts & Simpson 2002). In contrast, Kliakhandler, Davis & Bankoff (2001, referred to herein as KDB) consider the case where the film thickness is larger than the fibre radius, a situation that renders the assumption of small thickness invalid. They conducted experiments that revealed the richness of the dynamics of

https://doi.org/10.1017/S0022112006008706 Published online by Cambridge University Press

the flow down a vertical fibre and reported the existence of several flow regimes. They also proposed the use of a model evolution equation for the interface, which does not rely on the previously made lubrication-type assumptions. Their numerical solutions appear to be in reasonably good agreement with some, but not all, of their flow regimes. In particular, their model equation fails to capture a regime that features beads separated by relatively long flat thin-film regions.

In the present work, we revisit this problem with the aim of developing a theory capable of achieving better agreement with experimental observations. We derive an evolution equation for the total fluid radius using asymptotic reduction which assumes that the fluid radius is much smaller than its characteristic length (rather than the fibre radius) based upon a capillary lengthscale. We show that this equation is very similar to that used by KDB. We also show that numerical solutions of this equation yield good agreement with the experimental observations of KDB as well as those obtained as part of this work in terms of interfacial profiles, droplet spacings and velocities.

The rest of this paper is organized as follows. In § 2, we formulate the problem using a small parameter which is identified with the Bond number. The main evolution equation derived reduces naturally to those deduced using a thin film thickness limit and so a hierarchy of governing equations emerges. Travelling wave solutions and the results of transient numerical simulations are presented in § 3; a brief comparison with the experiments of KDB is also provided. Our experimental results are discussed in § 4 wherein we elucidate an instability that occurs in the wake of propagating widely spaced droplets; good agreement between our experimental data and modelling predictions is also demonstrated in this section. Finally, concluding remarks are provided in § 5.

2. Formulation

2.1. *Governing equations*

A Newtonian fluid, of constant viscosity μ and density ρ, flows vertically and axisymmetrically under gravity, whose acceleration is denoted by g, down a rigid circular fibre of radius $r = a$ whose axis is vertical (see figure 1). The vertical/axial coordinate is z and is measured such that it is positive as one moves down the fibre. The fluid ring is surrounded by an essentially inviscid gas whose dynamics will be neglected. The initial (equilibrium) radius of the fluid ring measured from the centre of the fibre is $r = \mathscr{R}$. We make no assumption about whether $(\mathscr{R} - a)/a \ll 1$ and we treat the problem as an axisymmetric fluid thread that contains a rigid cylindrical core. We therefore utilize scalings similar in spirit to those adopted in the long-wave theories of viscous fluid threads and jets (Papageorgiou 1995*a*, *b*) and compound jets (Craster, Matar & Papageorgiou 2002, 2005).

The film dynamics are governed by the Navier–Stokes equations in the fluid region:

$$u_t + uu_r + wu_z = -\frac{1}{\rho}p_r + \frac{\mu}{\rho}\left(u_{rr} + u_{zz} + \frac{1}{r}u_r - \frac{u}{r^2}\right), \tag{2.1}$$

$$w_t + uw_r + ww_z = g - \frac{1}{\rho}p_z + \frac{\mu}{\rho}\left(w_{rr} + w_{zz} + \frac{1}{r}w_r\right), \tag{2.2}$$

where t denotes time, u and w represent the radial and axial components of the velocity and p is the pressure. Note that unless stated otherwise, the subscript denotes

https://doi.org/10.1017/S0022112006008706 Published online by Cambridge University Press

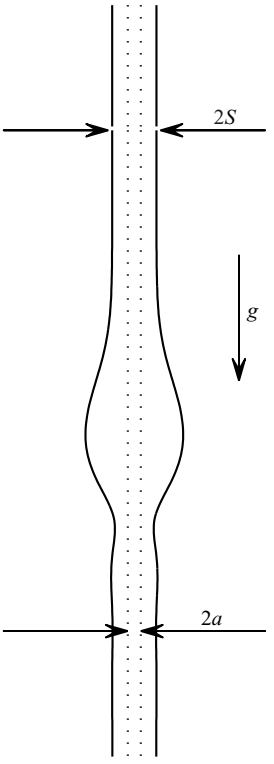


FIGURE 1. Schematic representation of the flow geometry.

partial differentiation. The equation of continuity is expressed by

$$\frac{1}{r}(ru)_r + w_z = 0. \tag{2.3}$$

On the surface of the fibre, $r = a$, we have no slip, that is, $u = w = 0$, while the normal and shear stress balances at the instantaneous location of the interface, $r = S(z, t)$, respectively, are

$$p - \frac{2\mu}{\left(1 + S_z^2\right)}\left(S_z^2 w_z - S_z(u_z + w_r) + u_r\right) = \gamma\left(\frac{1}{S\left(1 + S_z^2\right)^{1/2}} - \frac{S_{zz}}{\left(1 + S_z^2\right)^{3/2}}\right), \tag{2.4}$$

with a constant surface tension, γ, and

$$\left(1 - S_z^2\right)(u_z + w_r) + 2S_z(u_r - w_z) = 0. \tag{2.5}$$

Finally, we have the kinematic condition on the free surface:

$$S_t + wS_z = u. \tag{2.6}$$

2.2. *Scaling and asymptotic reduction*

The aim is to solve the above equations in the long-wavelength limit. We therefore assume that the radius of the fluid ring, $\mathscr{R}$, is much smaller than its characteristic length, $\mathscr{L}$, and render the above governing equations dimensionless by adopting the following scalings: $r = \mathscr{R}\hat{r}$, $z = \mathscr{L}\hat{z}$, $p = \rho g \mathscr{L}\hat{p}$, $t = \mathscr{L}\hat{t}/\mathscr{V}$, $w = \mathscr{V}\hat{w}$, $u = \epsilon\mathscr{V}\hat{u}$ where $\mathscr{V} \equiv \rho\mathscr{R}^2 g/\mu$. Notably, we choose our radial lengthscale to be that associated with the initial undisturbed radius of the fluid thread, not the fluid thickness or the fibre radius.

https://doi.org/10.1017/S0022112006008706 Published online by Cambridge University Press

The axial lengthscale, $\mathscr{L}$, is taken to be related to the capillary length so $\mathscr{L} = \gamma/\rho g\mathscr{R}$, and thus the dimensionless equations will not rely upon the fluid thickness being small relative to the fibre radius, but small relative to a dynamic lengthscale. Notably a non-dimensional group, the Bond number $Bo = \rho g\mathscr{R}^2/\gamma$, naturally appears and in the experiments this is typically small (~ 0.3 or so). The choice of lengthscale above sets $\epsilon = Bo$ and this is then implicitly a low-Bond-number, surface-tension-dominated, theory.

The dimensionless Navier–Stokes equations become (hereafter we drop the hat decoration and exclusively use dimensionless variables except where otherwise stated explicitly)

$$\epsilon^4 Re(u_t + uu_r + wu_z) = -p_r + \epsilon^2\left(u_{rr} + \epsilon^2 u_{zz} + \frac{1}{r}u_r - \frac{u}{r^2}\right), \tag{2.7}$$

$$\epsilon^2 Re\,(w_t + uw_r + ww_z) = 1 - p_z + \left(w_{rr} + \epsilon^2 w_{zz} + \frac{1}{r}w_r\right), \tag{2.8}$$

where the Reynolds number is defined as $Re = \rho\mathscr{V}\mathscr{L}/\mu$ and $\epsilon \equiv \mathscr{R}/\mathscr{L}$. We now assume that $\epsilon \ll 1$ and $Re = O(1)$ so that inertial contributions are removed henceforth. The equation of continuity remains unaltered.

The no-slip condition, $u = w = 0$, is imposed on $r = \alpha$ where $\alpha = a/\mathscr{R} < 1$ is a dimensionless ratio of the initial fluid radius to that of the fibre. Note that a small α corresponds to a thick, and $\alpha \to 1$ to a thin, fluid layer, relative to the fibre radius. The dimensionless normal stress balance at $r = S(z,t)$ is given by

$$p - \frac{2\epsilon^2}{\left(1+\epsilon^2 S_z^2\right)}\left(\epsilon^2 S_z^2 w_z - S_z(\epsilon^2 u_z + w_r) + u_r\right) = \left(\frac{1}{S\left(1+\epsilon^2 S_z^2\right)^{1/2}} - \frac{\epsilon^2 S_{zz}}{\left(1+\epsilon^2 S_z^2\right)^{3/2}}\right). \tag{2.9}$$

The dimensionless shear stress balance is written as

$$\left[\left(1-\epsilon^2 S_z^2\right)(\epsilon^2 u_z + w_r) + 2\epsilon^2 S_z(u_r - w_z)\right] = 0. \tag{2.10}$$

The kinematic boundary condition remains unchanged.

The leading-order radial and axial components of the Navier–Stokes equations are given by

$$p_r = 0, \quad p_z = 1 + \frac{1}{r}(rw_r)_r, \tag{2.11}$$

while the leading-order normal and tangential stress balances at the interface are

$$p = \frac{1}{S} - \epsilon^2 S_{zz}, \qquad w_r = 0. \tag{2.12}$$

A notable term which is included here is the $\epsilon^2 S_{zz}$ term in the pressure. Strictly speaking, the inclusion of this term may appear to be *ad hoc*, but it has logical claims for inclusion. It is the term of next order in ϵ^2 that involves the highest derivative and, as such, it is a singular perturbation suggesting that the S_{zz} term should be important. This is reflected in a linear analysis where the inclusion of this term is vital to ensure the correct high-wavenumber cutoff occurs; conventionally this term, or even the full curvature, is kept in long-wave theories of jets, threads and liquid bridges (Eggers & Dupont 1994; Garcia & Castellanos 1994; Ambravaneswaran & Basaran 1999) for these reasons and as its inclusion improves comparison with experiments. Moreover in those theories it is also possible to proceed using an alternative Galerkin method

https://doi.org/10.1017/S0022112006008706 Published online by Cambridge University Press

as detailed in the review by Eggers (1997) which then leads to a consistent rationale for retaining the full curvature.

Solving the equations above then yields an evolution equation for $S(z,t)$ given by

$$S_t + w(S,z,t)S_z = u(S,z,t), \tag{2.13}$$

wherein $u(S,z,t)$, $w(S,z,t)$ and $p(z,t)$ are given by

$$u(S,z,t) = \frac{(S^2[p_z-1])_z}{8S}\left[\alpha^2 - S^2 + 2S^2\log\frac{S}{\alpha}\right] - \frac{p_{zz}}{16S}(\alpha^2-S^2)^2, \tag{2.14}$$

$$w(S,z,t) = -\frac{1}{4}(p_z-1)\left[\alpha^2 - S^2 + 2S^2\log\frac{S}{\alpha}\right], \tag{2.15}$$

$$p = \frac{1}{S} - \epsilon^2 S_{zz}. \tag{2.16}$$

Note that we have utilized the no-slip condition at $r=\alpha$ in determining both u and w.

Equation (2.13) can be re-expressed as

$$8(S^2)_t = \frac{\partial}{\partial z}\left([p_z-1]\left[2S^2\left(\alpha^2 - S^2 + 2S^2\log\frac{S}{\alpha}\right) - (\alpha^2-S^2)^2\right]\right). \tag{2.17}$$

Inspection of this equation reveals that mass is indeed conserved by demanding that the solutions be periodic. We also note that with the exception of the ϵ^2 factor in the pressure, and the fact that those authors have also retained the full curvature term, (2.13)–(2.16) are identical to the model equation used by KDB; the difference is related to the choice of scalings in the present work.

The model also limits to evolution equations previously used in the literature. Notably, if $S(z,t) = \alpha + \eta(z,t)$, where $\eta \ll 1$, so that the film is thin relative to the fibre, one can expand (2.13) for small η to get

$$\left(1+\frac{\eta}{\alpha}\right)\eta_t + \frac{1}{3}\frac{\partial}{\partial z}\left[\eta^3\left(1+\frac{\eta}{\alpha}\right)\left(1+\frac{\eta_z}{\alpha^2(1+\eta/\alpha)^2} + \epsilon^2\eta_{zzz}\right)\right] = 0, \tag{2.18}$$

which is related to the thin-layer model of Roy *et al.* (2002); there is a difference in one of the terms (that multiplying the pressure gradient).

Since the equilibrium state has $S=1$ we have $0<\eta\leqslant 1-\alpha$ and thus this expansion and model are formally valid for small $1-\alpha$; it also conserves mass as the first term is $[(\eta+\alpha)^2-\alpha^2]_t/2$. Taking the leading term, so $(1+\eta/\alpha)\to 1$, one recovers the evolution equation of Frenkel (1992) as used by Kalliadasis & Chang (1994) and others:

$$\eta_t + \frac{1}{3}\frac{\partial}{\partial z}[\eta^3(1+\eta_z+\epsilon^2\eta_{zzz})] = 0, \tag{2.19}$$

which is valid either on the exterior, or interior, of a rigid wall at $r=\alpha$; note that the parameter α no longer appears explicitly in this equation, but is still present through the boundary conditions. Equation (2.19) also corresponds to that of Hammond (1983), to within a rescaling, when the gravitational term is absent, i.e.

$$\eta_t + \frac{1}{3}\frac{\partial}{\partial z}[\eta^3(\eta_z+\epsilon^2\eta_{zzz})] = 0. \tag{2.20}$$

Equation (2.13), which models the dynamics of the film down the vertical fibre, is parameterized by α and ϵ. In order to determine a value for α (from an experimental

https://doi.org/10.1017/S0022112006008706 Published online by Cambridge University Press

run, say) one needs to know the volumetric flow rate:

$$Q = 2\pi \int_{\alpha}^{S} rw \, \mathrm{d}r = 2\pi(p_z - 1)\left(\frac{(S^2-\alpha^2)(3S^2-\alpha^2)}{16} - \frac{S^4}{4}\log\frac{S}{\alpha}\right), \tag{2.21}$$

which, in dimensional variables for the equilibrium state, is given by

$$Q = 2\pi\frac{\rho g a^4}{16\mu\alpha^4}(-(1-\alpha^2)(3-\alpha^2) - 4\log\alpha); \tag{2.22}$$

recall that $\alpha < 1$ so Q is positive; thus given Q (easily measurable in the experiments) we get α and hence the equilibrium film radius $\mathscr{R}$, and similarly $\mathscr{L}$, from which ϵ follows.

With the non-dimensionalization above we make no statement about the fluid layer being thin relative to the fibre radius: the fibre radius plays no role in the non-dimensionalization of the governing equation. It only emerges as a parameter in the boundary conditions, α, and plays no role in the non-dimensional Navier–Stokes and stress and interface equations; it enters the model equations through the velocity field u and w.

3. Numerical results

We begin the presentation of our results by examining briefly the linear stability of (2.13) and comparing its predictions with those of the full Stokes flow problem as well as the thin-layer theory, (2.18). We then present travelling wave solutions of the flow followed by results from transient numerical simulations.

3.1. *Linear stability analysis*

We conduct a linear stability analysis by linearizing (2.13) about the following base state:

$$S = 1, \quad p = 1, \quad w = \frac{1}{4}\left[2\log\frac{1}{\alpha} - (1-\alpha^2)\right], \tag{3.1}$$

and adopting a normal mode approach: $S = 1 + \hat{S}\exp(\mathrm{i}kz + \lambda t)$ wherein $\hat{S}$ is the amplitude of the linear perturbation and k and λ are its (real) wavenumber and (complex) growth rate. This yields the following expression for λ:

$$\lambda = \frac{k^2}{16}(\epsilon^2 k^2 - 1)[(\alpha^2-1)^2 - 2(\alpha^2 - 1 - 2\log\alpha)] - \frac{\mathrm{i}k}{2}(\alpha^2 - 1 - 2\log\alpha); \tag{3.2}$$

this equation is identical to that of KDB except they have $\epsilon = 1$. The maximum real growth rate, λ_m, given by

$$\lambda_m = \frac{1}{64\epsilon^2}[2(\alpha^2 - 1 - 2\log\alpha) - (\alpha^2-1)^2], \tag{3.3}$$

occurs for $k_m = 1/\sqrt{2}\epsilon$; we call this the 'most dangerous mode'. This is not the same as that of a viscous Rayleigh jet, at zero Reynolds number, for which the $k = 0$ mode is most unstable (Chandrasekhar 1961). The cut-off wavenumber $k_c = 1/\epsilon$ for which the real growth rate is zero, however, corresponds to the classical Rayleigh–Plateau mode for the capillary instability of a viscous jet. Both the cut-off wavenumber, k_c, and most dangerous mode, k_m are short waves and strictly lie outside the range of validity of the long-wave model.

https://doi.org/10.1017/S0022112006008706 Published online by Cambridge University Press

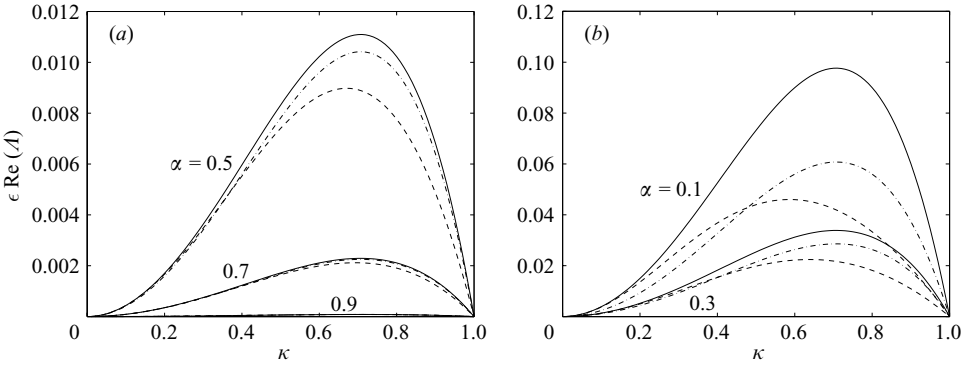


FIGURE 2. The variation of $\epsilon\,\mathrm{Re}\,(\Lambda)$ with κ (see the Appendix for definitions of Λ and κ and their relation to λ and k) for the different models. A comparison of the predictions of the Stokes flow equations (dashed lines) with those of the long-wave (solid lines) (3.2) and thin-layer (dot-dashed lines) (3.4) theories is shown for $0.5 \leqslant \alpha \leqslant 0.9$ in (*a*) and for $0.1 \leqslant \alpha \leqslant 0.3$ in (*b*).

As $\alpha \to 1$, (3.2) tends to

$$\lambda \sim \frac{k^2}{3}(1-\epsilon^2 k^2)(1-\alpha)^3, \tag{3.4}$$

which is the growth rate associated with the thin-layer models, (2.18) and (2.19).

In order to determine the range of α over which (2.13) provides a reasonably good approximation of the full equations, we determine the linear stability characteristics of the Stokes flow equations; these equations govern the flow in the absence of a disparity in scales between the radial and axial dimensions, that is $(r, z, h) \sim \mathscr{R}$ and $(u, w) \sim \mathscr{V}$. The details of this analysis can be found in the Appendix. In figure 2, we show dispersion relations obtained via solution of the Stokes flow problem and from long-wave theory for different α values. Inspection of this plot reveals that the predictions of long-wave theory are in excellent agreement with the solutions of the Stokes flow problem for $\alpha \geqslant 0.4$. The agreement, however, deteriorates for smaller α values. This may be related to the fact that the pressure becomes increasingly radially dependent with decreasing α. We also show in figure 2 the dispersion relations associated with the thin-layer models, (2.18) and (2.19). Although the agreement between thin-layer theory and the solutions of the Stokes flow problem deteriorates more rapidly for low $\kappa = \epsilon k$ (the curve for $\alpha = 0.1$ shows this, and detailed examination of the other curves shows similar behaviour albeit much less pronounced) it does, interestingly, appear to follow the dispersion curve globally, for say $\alpha = 0.5$, more closely than does the full long-wave model. In spite of this, we use (2.13) to examine the film dynamics in the remainder of this paper.

3.2. *Travelling wave solutions*

Experiments appear to show steadily propagating droplet or bead-like solutions that are sometimes separated by long thinner regions of constant radius (KDB). To investigate this further, we solve the governing equations by moving to a travelling wave coordinate, $\xi = z - ct$ where c is a constant wave speed to be determined. The unknown fluid radius is $S(z, t) = S(\xi)$ and we apply periodic boundary conditions at $\xi = \pm L/2$, where L represents the length of the computational domain; for a single-droplet solution L corresponds to the droplet–droplet spacing. Thus (2.13) becomes a nonlinear differential eigenvalue problem where S and c are determined for given

https://doi.org/10.1017/S0022112006008706 Published online by Cambridge University Press

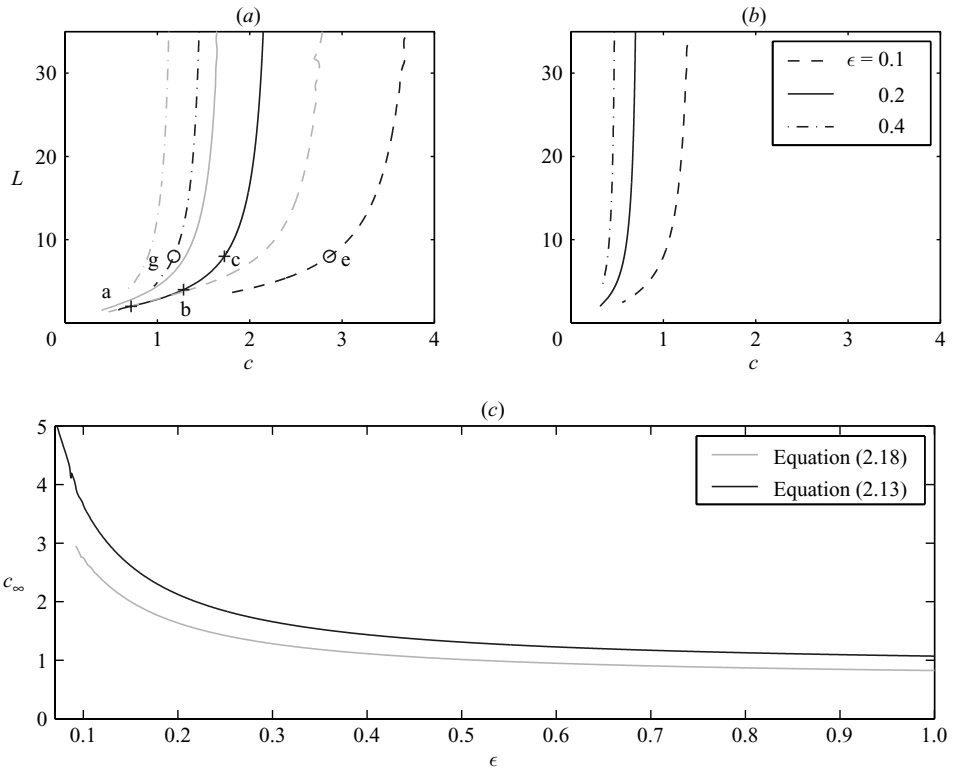


FIGURE 3. Travelling wave solutions: spacings and propagation speeds. (a, b) The droplet speed, c, versus domain length, L, for α=0.25 and 0.5, respectively, and various $\epsilon = 0.25$. In (a), the darker and lighter grey lines show the predictions of (2.13) and (2.18), respectively. The letters a,b, c, e and g in (a) refer to (L, c) combinations for which the profiles in figure 4 (the letters correspond to the panels in figure 4: f and c coincide) are computed. (c) A plot of c_∞ (the speed for a long L, here $L = 30$) versus ϵ for $\alpha = 0.25$.

L. This is achieved numerically using a Newton–Kantorovich approach with Fourier transforms providing the discretization in space, using n modes (typically n is either 256 or 512). We have n equally spaced gridpoints z_i, $i = 1 \ldots n$; however, there are $n+1$ unknowns: the radial values S_i, $i = 1 \ldots n$ (due to the spatial discretization) and the wave speed c. In order to fix c, we impose the following condition as a constraint on the fluid mass:

$$\int_{-L/2}^{L/2} (S^2(\xi) - \alpha^2)\, \mathrm{d}\xi = L(1 - \alpha^2). \tag{3.5}$$

One begins with a reasonable guess for the wave speed and profile, which via Newton iterations rapidly converges to the solution; continuation is then used to track this solution branch as parameters change.

Figure 3(a, b) shows the variation of the wave speed c with the domain length L for $\alpha = 0.25$ and 0.5. Here, ϵ is varied parameterically: $\epsilon = 0.1$, 0.2 and 0.4. It is evident that there is a trend such that solutions with smaller L travel slower than those with larger L, implying that relatively long waves eventually catch up with, coalesce and consume waves of shorter wavelength. It is also clear that the thinner layer of fluid, characterized by $\alpha = 0.5$, gives rise to droplets that propagate more slowly for the same domain length than in the $\alpha = 0.25$ case (see figure 3a): the curves

https://doi.org/10.1017/S0022112006008706 Published online by Cambridge University Press

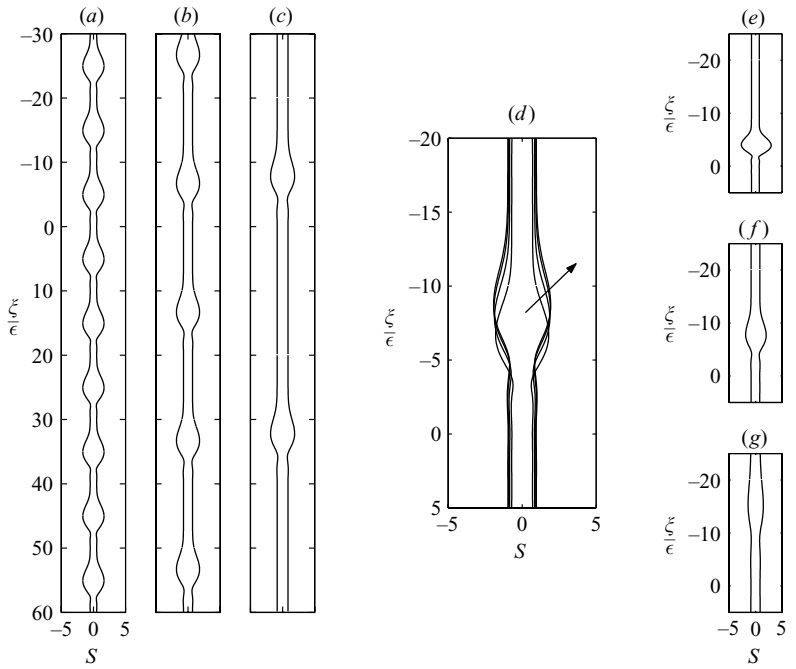


FIGURE 4. Profiles of travelling wave solutions. (*a*), (*b*) and (*c*) Periodically extended solutions for $L = 2, 4, 8$ for the points labelled 'a', 'b' and 'c' in figure 3, respectively. (*d*) The effect of altering L on the shape of the solutions shown here for $L = 4, 8, 16$ and 32 with the arrow indicating the direction of increasing L. In all these panels, $\alpha = 0.25$ and $\epsilon = 0.2$. (*e*), (*f*) and (*g*) The variation of the profiles for $L = 8$ and $\alpha = 0.25$ with ϵ; here, $\epsilon = 0.1, 0.2$ and 0.4, corresponding to the points labelled 'e', 'c' and 'g' in figure 3(*a*), respectively. The left (right) lines are profiles computed using (2.13) [(2.18)].

in figure 3*b* are shifted to the left with increasing α. This is due to the associated increase in viscous retardation, as expected. For given α and ϵ values, no travelling wave solutions could be found for a sufficiently small value of L. Inspection of figure 3 also reveals that c asymptotes to a value c_∞ for large L; the variation of c_∞ with ϵ in figure 3 (*c*) shows that c_∞ asymptotes to a constant value as $\epsilon \to 1$ (although the results for the relatively large ϵ should be treated with caution since the models are no longer valid in this range of parameters). Also shown in figure 3(*a*) (and figure 3*c*) is a comparison between the predictions of (2.13) and (2.18). Clearly, the thin-layer theory gives rise to similar trends to the long-wavelength model but underpredicts c for given α, ϵ and L. The speed c decreases as ϵ increases; the relative importance of surface tension decreases and the amplitude of the droplets also decreases so they contain less mass.

In figure 4(*a–c*), we show S profiles for three different (L, c) combinations designated by 'a', 'b', 'c' in figure 3(*a*). (Note that we plot ξ/ϵ rather than ξ in the ordinate axis.) These profiles all exhibit droplet or bead-like structures of varying spacing; there are small capillary ripples in the region wherein the beads adjust onto the preceding flat region. The wave solutions characterized by relatively large L and c values comprise beads that are separated by long, flat film regions of constant radius; the maximal film radius, however, appears to be relatively insensitive to variations in L and c. In figure 4(*d*), we show the effect of varying L on the solution profile with $\alpha = 0.25$ and $\epsilon = 0.2$; here c varies as these profiles are taken from points along the solid

https://doi.org/10.1017/S0022112006008706 Published online by Cambridge University Press

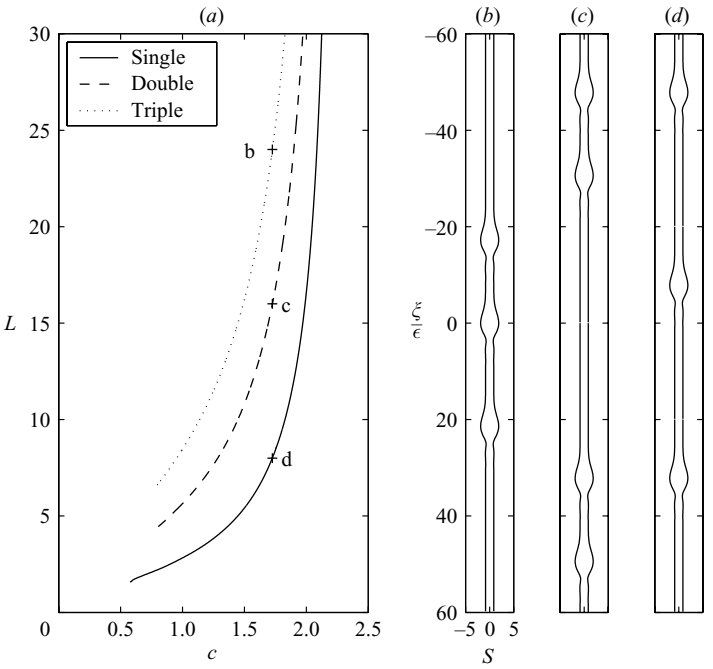


FIGURE 5. Non-uniqueness of solutions. (*a*) Length, L, versus speed, c, for single-, double- and triple-bead solutions. The computed profiles for the points labelled 'b', 'c' and 'd' are shown in (*b–d*), respectively. Here, $c = 1.73$, $\alpha = 0.25$, $\epsilon = 0.2$, as computed with $L = 24, 16$ and 8, respectively.

line in figure 3(*a*). Clearly, increasing L results in a small quantitative change in the profile but no qualitative variations. We have also investigated the effect of ϵ on the flow profiles. In figure 4(*e–g*), we show solutions for the points 'e', 'c' and 'g' in figure 3(*a*), which are characterized by $L = 8$ and $\alpha = 0.25$, and $\epsilon = 0.1$, 0.2 and 0.4, respectively; the predictions of (2.13) and (2.18) are shown. It is worth recalling that $\epsilon \equiv \mathscr{R}/\mathscr{L} = \rho g \mathscr{R}^2/\gamma$, which is a Bond number; thus increasing ϵ can be interpreted as a decrease in the relative significance of surface tension and gravitational forces. Inspection of figure 4(*e–f*) shows that the solutions become more bead-like with decreasing ϵ with more pronounced capillary waves in the 'adjustment' region. This is to be expected since the surface tension forces become significant in this case and drive a Rayleigh instability, which is responsible for the ultimate breakup of a capillary thread. For larger ϵ values, gravitational forces are relatively dominant and the solutions vary more smoothly over a wider range of the spatial domain and exhibit much less pronounced peaks. The thin-layer model predictions are very similar to those of (2.13) despite the relatively large difference in the predicted c values (see figure 3*a*), although, once again, the results for the larger ϵ values should be interpreted with caution since they may be outside the range of validity of the models.

Equation (2.13) also exhibits non-uniqueness of solutions. Figure 5(*b–d*) shows three solutions of different spacing, travelling at the same speed c, having the same α and ϵ values; these correspond to the points marked 'b', 'c' and 'd' in figure 5(*a*). For a given spatial interval, it is evident that the (periodically extended) travelling wave solutions shown in figure 5(*b–d*) have three, two and a single bead respectively. (An experimental

https://doi.org/10.1017/S0022112006008706 Published online by Cambridge University Press

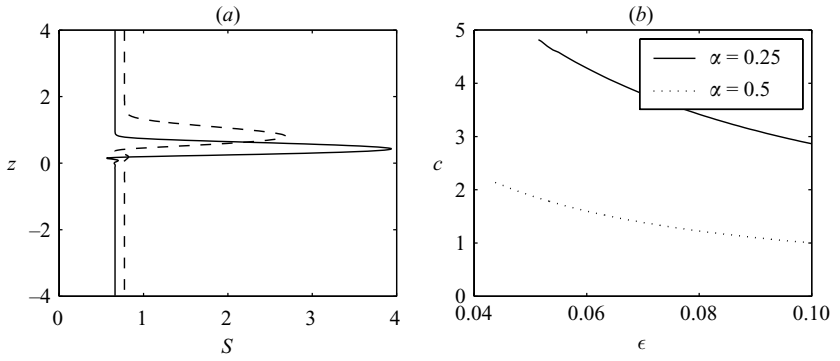


FIGURE 6. Disappearance of the travelling wave solution: (*a*) two profiles for $\epsilon = 0.05$ (solid line) and 0.1 (dashed line) with $\alpha = 0.25$, and (*b*) the variation of the velocities with ϵ for two different α values. $L = 10$.

Regime	α	ϵ	c_{expt}	L	c	$h_{\max}$ (mm)	h_{expt} (mm)	$\mathscr{L}$ (mm)
(a)	0.2551	0.2915	1.1698	5.81	1.195	1.51	1.47	3.4
(b)	0.2856	0.233	0.3200	1.637	0.656	1.29	1.02	3.7
(c)	0.3262	0.178	0.9318	8.185	1.36	1.41	1.20	4.3

TABLE 1. A comparison of the experimental and theoretical values for the spacings and propagation speeds for the values of α and ϵ corresponding to the experimental observations of KDB shown in figure 7.

photograph showing a periodically spaced two-pulse family, which bears structural similarity to the numerical solutions depicted in figure 5*c*, is shown in figure 13 below.) Solution non-uniqueness is also a feature of related models which describe the dynamics of falling planar films (Chang & Demekhin 2002) or on rotating disks (Sisoev, Matar & Lawrence 2003). Therefore it is important to recognize the possibility that there can exist flow regimes which are not just regularly spaced single droplets.

One feature that clearly emerges is that the travelling wave solution ceases to exist below a critical value of ϵ (see figure 6), which is consistent with earlier studies of the simpler model equation (2.19). In that case, one can rescale that equation to absorb both ϵ and α into a single control parameter and, via matched asymptotic expansions (Kalliadasis & Chang 1994; Chang & Demekhin 1999), show that the pulse-like waves on an infinite domain disappear for a critical value of the control parameter and the wave speed tends to infinity as this is approached. Here, we witness exactly the same phenomenon: as ϵ is decreased the amplitude of the pulses and their velocity grow dramatically (see figure 6*a*) until the system can no longer support drops of such magnitude and solutions cease to be found numerically (or analytically, Kalliadasis & Chang 1994; Chang & Demekhin 1999).

It is now possible to briefly compare with the experimental results of KDB: one can identify the observed droplet spacing with L and then compute the corresponding c and droplet profile. The results are shown in figure 7 and table 1 (it is notable that the choice of lengthscale $\mathscr{L}$ is similar to that of the observed droplet lengths) in which we plot the computed profiles in dimensional form and list the calculated droplet speed c and maximal film thickness, $h_{\max}$, respectively. For the longer spaced solutions (see figure 7*a*), which correspond to KDB's 'regime (a)', the agreement is excellent.

https://doi.org/10.1017/S0022112006008706 Published online by Cambridge University Press

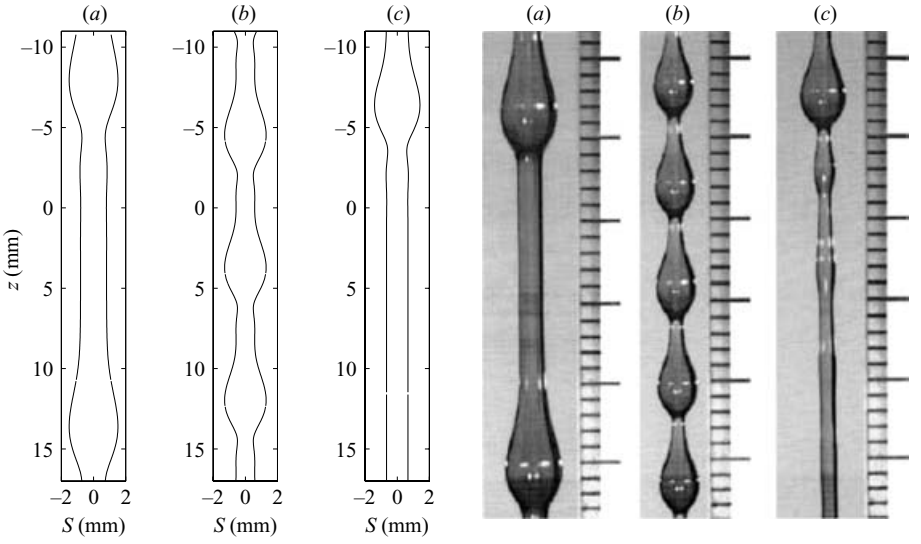


FIGURE 7. Comparison with experiments. (*a–c*) Computed profiles for regimes 'a', 'b' and 'c' of KDB, cf. their figure 1, which is reproduced on the right of this figure. The parameter values for the experimental and numerically predicted profiles are shown in table 1.

We note that this regime could not be predicted using the model equation proposed by KDB. The agreement with their 'regime (c)' (see figure 7*c*) is also good. For the closer spaced beads (see figure 7*b*) corresponding to their 'regime (b)', the shortest domain on which solutions could be found were $L = 2.16$ for which the calculated c (see table 1) is approximately twice the observed value. In fact our experiments performed later suggest that regime (b) is not a steady regime: we observed closely spaced droplets near the inlet which sometimes persisted over a considerable length before coalescence gave way to regime (a) and we therefore discount this regime; the comparison with regime (b) is just given for completeness. Regime (c) is also not steady as the large droplet is actually consuming the much smaller stationary droplet ahead and in the experiments, and numerical simulations detailed later, one clearly observes the large droplet to oscillate slightly; one could consider this a perturbation to a steadily propagating droplet.

3.3. *Transient simulations*

The steadily propagating solutions have given insight into the range of travelling droplet solutions that exists. There are clearly families of solutions, but the steady analysis does not indicate whether any particular family is naturally selected. To elucidate this, we perform numerical simulations of (2.13) over large times and on relatively long domains. The numerical method employed to carry out the computations uses Fourier transforms for spatial discretization (with 256–1024 modes) and an implicit Gear's method in time; periodic boundary conditions are imposed. In order to inspire confidence in the performance of the numerical method, we have ensured that its predictions are in excellent agreement with those of linear theory and that mass is conserved.

Starting from a layer of uniform radius seeded with pseudo-random-noise disturbances drawn from a uniform distribution in the range $(-10^{-4} : 10^{-4})$ on relatively short spatial domains, 'convergence' to steadily propagating solutions is achieved. An example of this is shown in figure 8 for $t = 100$, $-\pi < z < \pi$ and various α and ϵ

https://doi.org/10.1017/S0022112006008706 Published online by Cambridge University Press

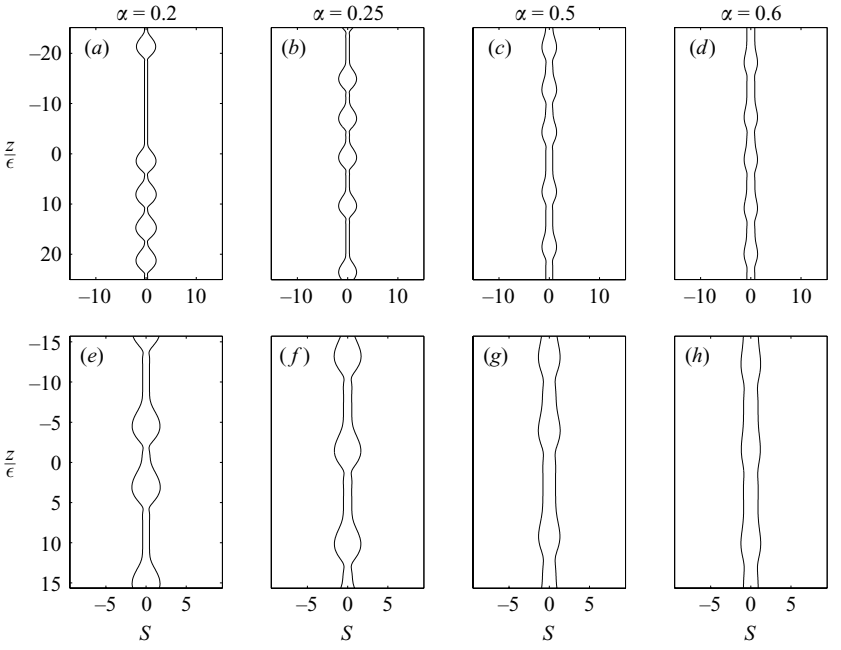


FIGURE 8. 'Steady' solutions shown at $t = 100$ obtained via transient numerical simulations of (2.13) starting from $S = 1$ perturbed by small-amplitude pseudo-random disturbances. The results in (*a–d*), and (*e–h*) were generated with $\epsilon = 0.125$ and $\epsilon = 0.2$, respectively.

values. We note that for certain parameters, co-existence of travelling wave solutions of different 'families' (featuring closely and widely spaced beads) is observed (see, for instance, figure 7*b*, *c*); this is to be expected considering the results discussed in § 3.2. As can also be seen in figure 7, increasing the average film radius (or decreasing the fibre radius) by decreasing α leads to the formation of more pronounced, closely spaced beads; a similar trend is also observed upon decreasing ϵ, which increases the relative significance of the surface tension forces. It is also notable that when plotted as S versus z the droplets have a non-dimensional length of order unity which suggests that the choice of lengthscale in the non-dimensionalization is the appropriate one.

We have also examined the film evolution for relatively large spatial domains ($-5\pi < z < 5\pi$) initiated by pseudo-random disturbances of the same amplitude as discussed earlier, and over long time intervals (up to $t = 1000$). In figure 9(*a*), we show a space–time plot, which reveals that larger amplitude beads flowing down the fibre coalesce with preceding smaller, slower moving droplets; these features are also present in simulations of the simpler model equations, (2.18) and (2.19), see Kerchman & Frenkel (1994), Kalliadasis & Chang (1994), Chang & Demekhin (1999), Roy, Roberts & Simpson (2002). Figure 9(*b*) shows the solution at $t = 650$ over the entire domain, while a 'zoom-in' on the interval $-30 \leqslant z/\epsilon \leqslant 60$ is provided in figure 9(*c*); these plots clearly show the larger bead at $z/\epsilon = 32$ and the fact that small-amplitude waves become apparent in its 'wake'. These results reveal the complex dynamics which accompany the flow of a film down a vertical fibre and, importantly, the competition between the coarsening effect brought about by bead coalescence and the transition to smaller scales that arises due to the instability in the relatively flat regions upstream

https://doi.org/10.1017/S0022112006008706 Published online by Cambridge University Press

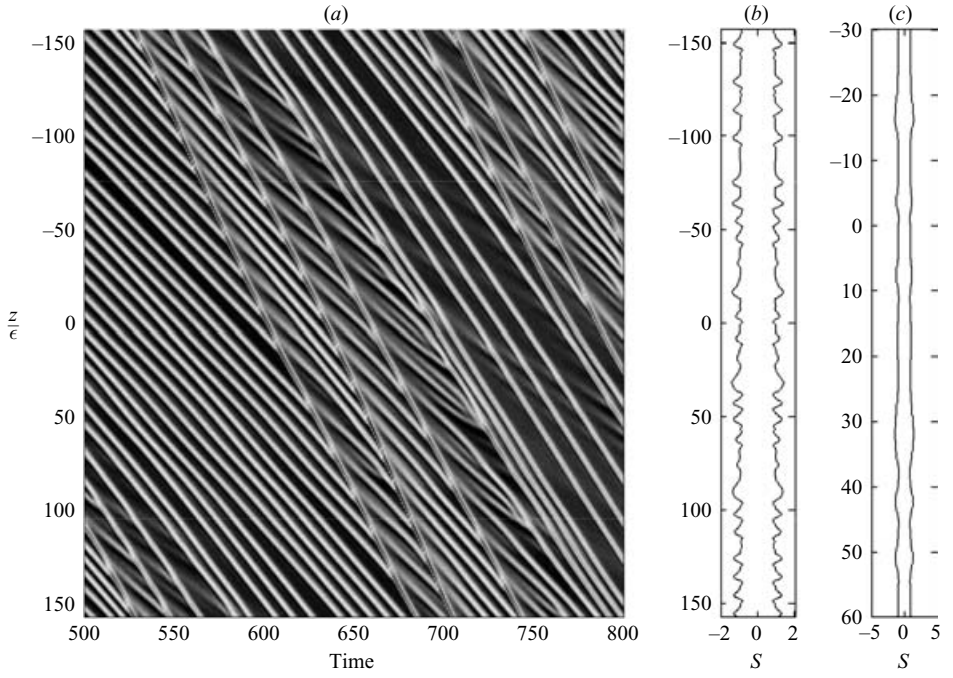


FIGURE 9. (*a*) A space–time plot illustrating the complex dynamics accompanying a typical film evolution with $\alpha = 0.6$ and $\epsilon = 0.2$, in which the light and dark shading indicate elevated and depressed regions, respectively. The crossing of the lines signifies the coalescence of a fast moving large bead with a slower moving smaller droplet located downstream. (*b*) The S profile at $t = 650$. (*c*) A 'zoom-in' on the $-30 \leqslant z/\epsilon \leqslant 60$ interval.

of the large structures. Thus, although there are regions in space where it almost appears that there is convergence to a steady solution, this is not the case.

We have also investigated situations characterized by very small ϵ values wherein surface tension provides the dominant driving force, by using travelling wave solutions perturbed by pseudo-random-noise disturbances (of amplitude $(-10^{-2} : 10^{-2})$) as initial conditions in our transient simulations. Thus the initial condition is that of a single droplet propagating at known speed c on a length L with superimposed pseudo-random noise; the transient code is adjusted to be in a moving coordinate frame, i.e. $\xi = z - ct$ and $S(z, t) = S(\xi, t)$, translating at the speed c of the unperturbed droplet. The length of the domain, $L = 2\pi$, is chosen to be several times that of the wavelength associated with the most dangerous linear mode. Periodic boundary conditions are applied, so this models the evolution of a train of steadily propagating droplets. The low values of ϵ give rise to solutions featuring spatial regions of rapid variation. In order to fully resolve these solutions, therefore, we utilize 1024 Fourier modes in space; detailed checks of mass conservation were used and convergence upon mesh refinement was also verified in order to confirm the accuracy of the numerical simulations. In figure 10, we show the results from a simulation with $\alpha = 0.4$ and $\epsilon = 0.05$ rendered as a space–time plot. The flat film on either side of the large bead is linearly unstable and, therefore, prone to the formation of small-amplitude droplets. The propagating larger bead consumes these growing droplets leaving behind a flat film. As will be discussed below, this is reminiscent of the experimental observations made as part of the present work. Also notable from figure 10 are the small-amplitude

https://doi.org/10.1017/S0022112006008706 Published online by Cambridge University Press

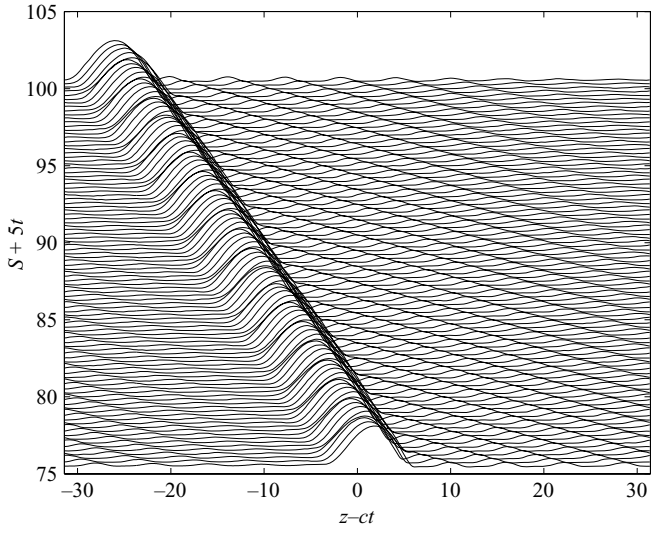


FIGURE 10. A space–time plot showing the film evolution with $\alpha = 0.4$ and $\epsilon = 0.05$ for $15 \leqslant t \leqslant 20$ in a translating frame; here, $L = 2\pi$, $c = 1.54$.

back and forth oscillations of the main bead. These are caused by its consumption of the smaller droplets ahead which increase its mass and velocity slightly. The bead then appears to shed mass and decelerate, which re-initiates the instability in the flat film behind it. The space–time plots are in the moving frame and indicate that these oscillating beads propagate more slowly than the steadily propagating ones.

4. Experimental results

Here, we present the results of our brief experimental study. Our primary focus is upon the well-separated droplet regime that the theory of KDB was unable to capture, and upon the situation when the main droplet is unstable. It is notable that we never observed regime (b) of KDB except near the inlet. A comparison between our numerical simulations and experimental observations is also provided.

4.1. *Setup*

KDB provide a brief experimental study of the flow using castor oil and, in § 3.2, we provided a comparison with their experimental observations. To gain further insight into the film dynamics, we have conducted our own experiments using silicone oil (Dow Corning 500 cS coloured with small amounts of Sudan II) of kinematic viscosity $\nu = 5\,\mathrm{cm}^2\,\mathrm{s}^{-1}$, surface tension $20.4\,\mathrm{dyn\,cm}^{-1}$ and density $0.97\,\mathrm{g\,cm}^{-3}$, flowing down nylon fishing line (of two diameters 0.53 mm and 0.25 mm); here, for brevity we primarily report the results associated with the 0.25 mm diameter fibre. Fixed flow rates were achieved using a gravity feed from a large container; the flow rates are very small, the largest being $Q = 0.07\,\mathrm{cm}^3\,\mathrm{s}^{-1}$. The fluid drained into a small container that was regularly weighed using a jeweller's balance (accurate to ± 0.005 g). The photographs were taken with a 3 MegaPixel Canon digital camera with video clips fed into a standard PC from which the velocity of the beads was readily extracted.

4.2. *Observations*

For $Q = 0.01\,\mathrm{cm}^3\,\mathrm{s}^{-1}$, $\alpha = 0.17$, and $\epsilon = 0.25$, we observed the rapid growth of small perturbations originating from the inlet into a fine structure of droplets. Many

https://doi.org/10.1017/S0022112006008706 Published online by Cambridge University Press

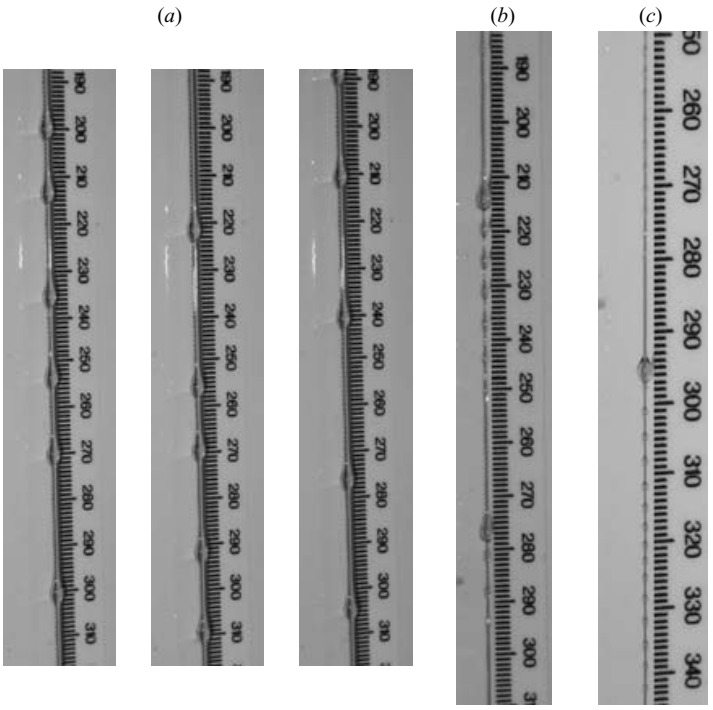


FIGURE 11. Experimentally observed profiles obtained for a fibre diameter of 0.25 mm. The flow rate is $Q = 0.01\,\mathrm{cm^3\,s^{-1}}$ in (a) and $Q = 10^{-4}$, $10^{-5}\,\mathrm{cm^3\,s^{-1}}$ in (b) and (c), respectively. The profiles shown in (a) were taken at time intervals separated by 5 s.

of these droplets undergo coalescence with preceding drops and then propagate more rapidly due to the associated increase in their mass. A more regular structure emerges approximately 1 m from the inlet: isolated droplets of similar shape propagate down the fibre with variable spacing, but at very similar speeds (see figure 11a–c). Occasionally, a large bead emerges and consumes smaller neighbouring droplets in its immediate downstream vicinity with new droplets emerging in its 'wake'.

At lower flow rates, one observes a very closely spaced 'beads on a string' structure over a distance of 1 m from the inlet, propagating slowly. As this 'chain' of beads progresses further downstream, the gap between the droplets increases and the droplets consume each other, grow in magnitude and propagate more rapidly. Typically, a single bead becomes dominant and consumes the droplets ahead leaving, once again, a flat film in its wake from which a new set of closely spaced, slowly moving droplets emerges (this behaviour is noticeable for $Q \sim 10^{-4}\,\mathrm{cm^3\,s^{-1}}$). An aesthetically appealing regular sequence of large drops propagating down the fibre with the flat film behind nucleating new droplets emerges of which figure 11(b) is an example. Here, the droplet at 270 mm leaves a flat film in its wake which is unstable and upon which the instability has time to grow until it is clearly visible; these small droplets move very slowly and the faster propagating large droplet at 210 mm is about to consume them. It then leaves a flat film behind and the process is repeated. As the flux is decreased further, the large droplets become less frequent, and the string of very slowly propagating droplets left in their wake remain for long periods (see figure 11c).

The results shown in figure 11 can be rationalized via inspection of figure 12, which shows the variation of α with ϵ as a result of altering Q. An increase in Q gives rise to

https://doi.org/10.1017/S0022112006008706 Published online by Cambridge University Press

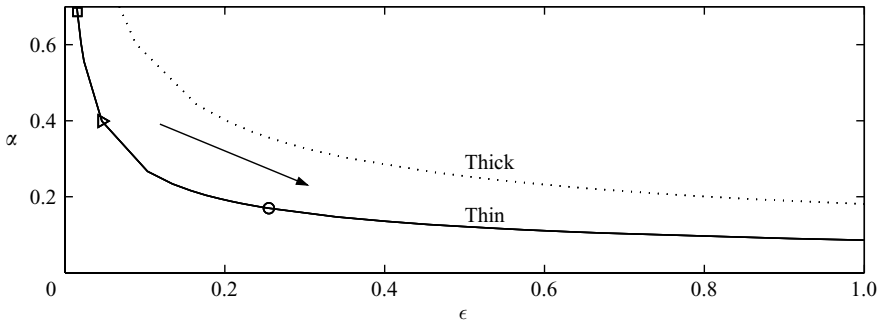


FIGURE 12. The variation of α with ϵ for varying Q; the arrow shows the direction of increasing Q. The points labelled with a circle, triangle and square correspond to $Q = 10^{-2}, 10^{-4}$ and $10^{-5}\,\mathrm{cm^3\,s^{-1}}$ and the profiles shown in panels (a), (b) and (c) of figure 11, respectively. The curves labelled 'Thin' and 'Thick' correspond to fibre diameters of 0.25 mm and 0.53 mm, respectively.

thicker films, smaller α and larger ϵ values, which implies a decrease in the significance of capillarity in relation to gravitational forces. As indicated in figure 12, a value of $Q = 10^{-2}\,\mathrm{cm^3\,s^{-1}}$ leads to small α and large ϵ values, implying a gravity-dominated situation and explaining the emergence of the steadily propagating, regularly-spaced bead regime shown in figure 11(a). The regimes characterized by regular droplets, with a long intervening flat film that becomes unstable, shown in figure 11(b, c), corresponds to smaller flow rates and, consequently, smaller ϵ and large α values, which is a surface-tension-dominated flow regime. Note that altering the fibre radius and/or the surface tension gives rise to different curves of similar shape (see figure 11) and that variation of the viscosity has a similar effect to altering the flux: decreasing ν increases Q and ϵ, and decreases α. The lengthscale $\mathscr{L} = \gamma/\rho g\mathscr{R}$ in each of the experiments shown in figure 11 is 4.6, 6.9 and 10 mm for (a), (b) and (c), respectively, which is broadly the lengthscale over which one expects surface tension to act, i.e. over a droplet.

The observed behaviour for the flow down the thicker fibre was very similar to that associated with the thinner one and some typical photographs are shown in figure 13. In figure 13(a) of this figure, we show an experimental profile of the film thickness for $Q = 0.07\,\mathrm{cm^3\,s^{-1}}$, $\alpha = 0.25$ and $\epsilon = 0.75$, which is arguably outside the asymptotic regime of the model; nonetheless the estimate of c, $c \sim 5.5\,\mathrm{cm\,s^{-1}}$, taken from a single pulse on an effectively infinite computational length, compares reasonably with the experimental value of $4.8\,\mathrm{cm\,s^{-1}}$ (for this case $\mathscr{L} = 2$ mm). The other panels in figure 13 show the development of a two-pulse periodic family that appeared at lower Q; panel (c) being an enlargement of (b) illustrates more clearly the small capillary droplets just ahead of the leading droplet. Upon decreasing the flux further, one sees the formation of the leading droplet from the largest unstable drop created by the flat-layer instability. Subsequently, this pair of larger droplets propagated down together with the leading droplet consuming smaller ones along its path.

In contrast to KDB, we did not witness distinct regimes, but more a gradual trend in the data. For instance, we only saw their regime (b) near the inlet and we view this as a transient feature. The steady, well-spaced, travelling droplets of their regime (a) are seen almost exclusively, but with a gradual transition as the flux decreases to more widely spaced droplets. Eventually, the long flat film between the droplets becomes

https://doi.org/10.1017/S0022112006008706 Published online by Cambridge University Press

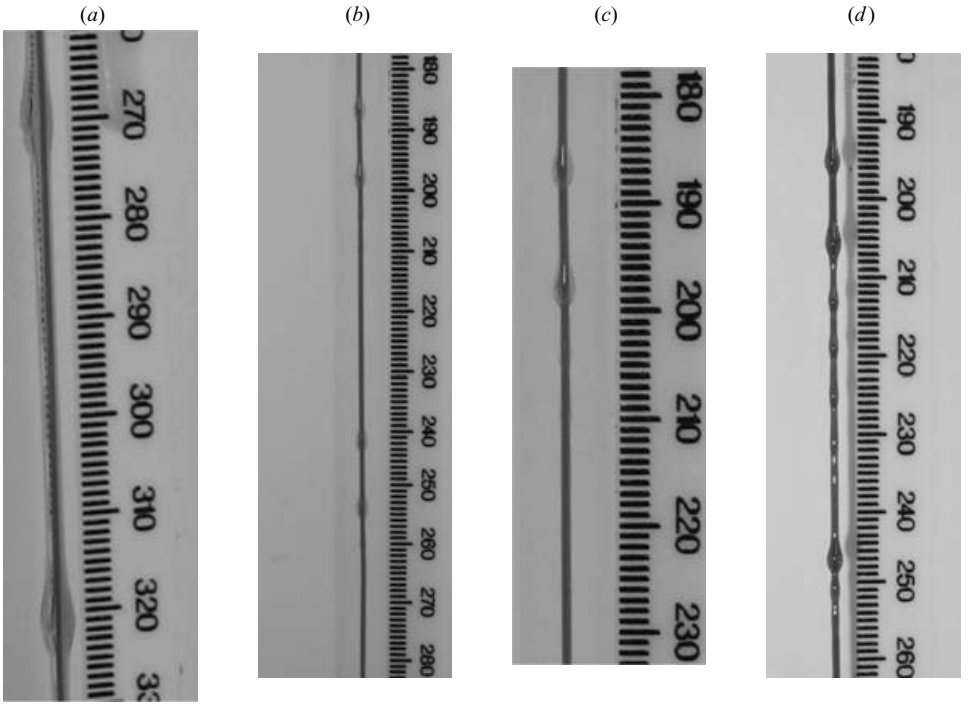


FIGURE 13. Typical experimental profiles for the 'thick' fibre. (*a*) A high flux case, $Q = 0.07\,\mathrm{cm^3\,s^{-1}}$. (*b–d*) Experiments at lower Q, $Q \sim 10^{-4}\,\mathrm{cm\,s^{-1}}$.

itself unstable and the instability has time to visibly grow. These small stationary droplets are then consumed by the travelling droplets; the increase in mass upon consumption caused a slight increase in velocity and the slight thinning just behind the droplet then causes it to decelerate leading to visible oscillations; this is then regime (c) of KDB.

4.3. *Comparison with theory*

In figure 14(*a*, *b*), we show a profile of the film radius obtained from our experiments and a numerical prediction determined via a travelling wave solution of (2.13); the parameter values are the same as those used to generate figure 11 (as indicated by the circle on the curve marked 'Thin' in figure 12). Inspection of these panels reveals relatively good agreement between theory and experiment in terms of interfacial profile. The predicted speed is $c = 2.4\,\mathrm{cm\,s^{-1}}$, which is also in reasonably good agreement with the experimentally measured value of $c = 2.08^{-1}\mathrm{cm\,s^{-1}}$. Note that the travelling wave solution is taken to be the single-droplet solution on an effectively infinite ($L = 20$) domain; there is a unique single-droplet solution for that problem. The length of the computational domain, cf. figure 3, is not an important parameter as the speeds asymptote to a fixed value and this therefore provides a predictive upper bound upon the experimental droplet velocity.

Next, we provide numerical predictions for the parameter values corresponding to those indicated by the square and triangle in figure 12, that, in turn, correspond to large α and small ϵ values (implying a surface-tension-dominated regime) for which the experimental profiles are shown in figure 11(*b*, *c*). In figure 14(*c*, *d*), we show interfacial profiles which are solutions of (2.13); these were obtained in a similar

https://doi.org/10.1017/S0022112006008706 Published online by Cambridge University Press

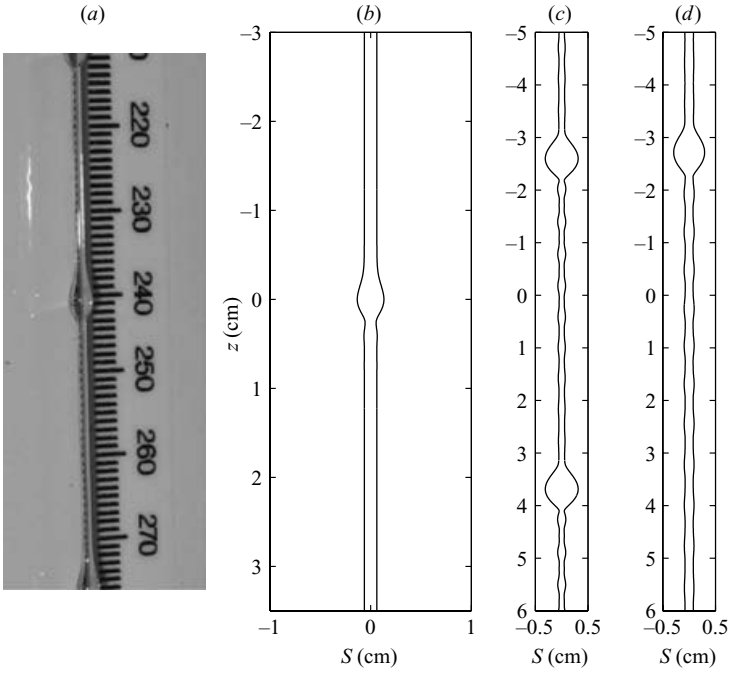


FIGURE 14. A comparison of an experimental profile (for the thin fibre) characterized by $\alpha = 0.17$ and $\epsilon = 0.254$, (*a*), with the corresponding steady solution of (2.13) cast in dimensional variables, (*b*), generated numerically with $L = 20$. (*c*, *d*) Computed profiles obtained via transient numerical solutions of (2.13) with $\alpha = 0.4$ and $\epsilon = 0.05$, and $\alpha = 0.7$ and $\epsilon = 0.025$, respectively, and the same initial conditions as for figure 10.

manner to those shown in figure 10. Comparison of figures 14(*c*) and 14(*d*) with 11(*b*) and 11(*c*), respectively, reveals that the salient features observed in the experiments are captured by our model. Particularly apparent are the small-scale oscillations in the relatively flat regions upstream and downstream of the prominent beads. These are driven by a linear instability of the flat regions: the wavelength of the small-scale droplets in figure 14(*c*, *d*) is the same as that associated with the most dangerous linear mode for this set of parameter values. These droplets are then consumed by the larger, faster-moving bead, which leaves behind a thin flat film that, once again, is vulnerable to a linear instability and the nucleation of small-scale droplets and so on. At the end of the previous section we noted that in the simulations the large beads oscillated slightly as they consumed the droplets downstream; this behaviour is also visible in the experiments.

5. Concluding remarks

We have conducted a study of flow down a vertical fibre and derived an evolution equation for the interface using long-wave theory parameterized by a dimensionless thickness parameter, α, and an aspect ratio, ϵ; making use of the capillary lengthscale, we identify ϵ as the Bond number. The main assumption underlying our model is that the characteristic radius of the total fluid is much smaller than the capillary lengthscale, that is, ϵ is small. The evolution equation we derived reduces to those previously used in the literature, based on the thin-layer limit, that assume the film

https://doi.org/10.1017/S0022112006008706 Published online by Cambridge University Press

thickness to be much smaller than the fibre radius; our model is similar to the equation used by KDB (except in the curvature).

We observe travelling waves that are obtained via the solution of a nonlinear eigenvalue problem, where the eigenvalue corresponds to the speed of propagation. The effect of system parameters on the structure, spacing and speed of these solutions was analysed; an interesting point is that the equations allow for a multiplicity of solutions. The model equations lead to widely spaced droplet solutions similar to those found in experiments. These results, along with those obtained from transient numerical simulations using a spectral method, compare reasonably with our experimental data, as well as other results available in the literature.

Appendix. Linear stability of the Stokes flow problem

Here, we perform a linear stability analysis of the Stokes equations which govern the flow of a film down a vertical fibre in the absence of a disparity in scales between the radial and axial coordinates. To this end, we scale z on $\mathscr{R}$ rather than $\mathscr{L}$ so that the governing equations become $\nabla p = \nabla^2 \boldsymbol{u}$ and $\nabla \cdot \boldsymbol{u} = 0$, with no shear stress and the usual normal stress conditions at the interface, and no-slip on the fibre surface. We conduct a linear stability analysis of these equations via the following linearization:

$$p = \frac{1}{\mathrm{Bo}} + \hat{p}, \quad u = \hat{u}, \quad S = 1 + \hat{S}, \quad w = w_0(r) + \hat{w}, \tag{A 1}$$

where $\mathrm{Bo} \equiv \rho g \mathscr{R}^2/\gamma$ is a Bond number and the hatted variables denote small perturbations; the base-state axial velocity is given by

$$w_0(r) = \frac{1}{4}\left(2\log\frac{r}{\alpha} - (r^2 - \alpha^2)\right). \tag{A 2}$$

The perturbation quantities satisfy

$$\nabla \hat{p} = \nabla^2 \hat{\boldsymbol{u}}, \quad \nabla \cdot \hat{\boldsymbol{u}} = 0, \tag{A 3}$$

subject to

$$\hat{u} = \hat{w} = 0 \quad \text{on} \quad r = \alpha, \tag{A 4}$$

$$\hat{p} - 2\hat{u}_r = -\frac{1}{Bo}(\hat{S} + \hat{S}_{zz}), \quad \hat{w}_r + \hat{u}_z = \hat{S}, \quad \hat{S}_t + w_0(1)\hat{S}_z = \hat{u}(1), \quad \text{on} \quad r = 1. \tag{A 5}$$

Note that the term $\hat{S}_{zz}$ remains in the pressure, cf. the discussion about the retention of $\epsilon^2 S_{zz}$ following equation (2.12).

The perturbed quantities are then expanded using normal modes:

$$(\hat{u}, \hat{w}, \hat{p})(r, z, t) = (\tilde{u}, \tilde{w}, \tilde{p})(r)\exp(\mathrm{i}\kappa z + \Lambda t), \quad \hat{S} = \tilde{S}\exp(\mathrm{i}\kappa z + \Lambda t), \tag{A 6}$$

where κ and Λ are the (real) wavenumber and (complex) growth of the perturbations, respectively. The scaling for z (and implicitly for time) adopted here, which is different from that used in the main text, implies that $\kappa = k\epsilon$ and $\Lambda = \lambda\epsilon$, ($k$ and λ are the wavenumber and growth rate for long-wave theory, respectively) and that $Bo = \epsilon$. Then one can map between the long-wave and the Stokes flow solutions with no free parameters.

https://doi.org/10.1017/S0022112006008706 Published online by Cambridge University Press

The solutions for $\tilde{u}$, $\tilde{w}$ and $\tilde{p}$ are obtained in terms of Bessel functions:

$$\tilde{u} = \frac{a_1}{2\kappa}(\kappa r I_0(\kappa r) - 2I_1(\kappa r)) + a_2 I_1(\kappa r) + \frac{a_3}{2\kappa}(\kappa r K_0(\kappa r) + 2K_1(\kappa r)) - a_4 K_1(\kappa r), \quad (A\,7)$$

$$\tilde{w} = \frac{\mathrm{i}a_1}{2} r I_1(\kappa r) + \mathrm{i}a_2 I_0(\kappa r) - \frac{\mathrm{i}a_3}{2} r K_1(\kappa r) + \mathrm{i}a_4 K_0(\kappa r), \quad (A\,8)$$

$$\tilde{p} = a_1 I_0(\kappa r) + a_3 K_0(\kappa r). \quad (A\,9)$$

Substitution of (A 7)–(A 9) into (A 4) and (A 5) ultimately leads to a characteristic equation for the growth from which it is possible to construct dispersion relations for the real part of the growth rate as a function of the wavenumber. A comparison of these dispersion relations with those obtained from long-wave theory is shown in figure 2 for different values of α.

REFERENCES

Ambravaneswaran, B. & Basaran, O. A. 1999 Effects of surfactants on the nonlinear deformation and breakup of stretching liquid bridges. *Phys. Fluids* **11**, 997–1015.

Chandrasekhar, S. 1961 *Hydrodynamic and Hydromagnetic Stability*. Oxford University Press.

Chang, H.-C. & Demekhin, E. A. 1999 Mechanism for drop formation on a coated vertical fibre. *J. Fluid Mech.* **380**, 233–255.

Craster, R. V., Matar, O. K. & Papageorgiou, D. T. 2002 Pinchoff and satellite formation in surfactant covered viscous threads. *Phys. Fluids* **14**, 1364.

Craster, R. V., Matar, O. K. & Papageorgiou, D. T. 2005 Compound threads with large viscosity contrasts. *J. Fluid Mech.* **533**, 95–124.

De Ryck, A. & Quéré, D. 1996 Inertial coating of a fibre. *J. Fluid Mech.* **311**, 219–237.

Eggers, J. 1997 Nonlinear dynamics and breakup of free-surface flows. *Rev. Mod. Phys.* **69**, 865–929.

Eggers, J. & Dupont, T. F. 1994 Drop formation in a one-dimensional approximation of the Navier-Stokes equation. *J. Fluid Mech.* **262**, 205–221.

Frenkel, A. L. 1992 Nonlinear theory of strongly undulating thin films flowing down vertical cylinders. *Europhys. Lett.* **18**, 583–588.

Garcia, F. J. & Castellanos, A. 1994 One dimensional models for slender axisymmetric viscous jets. *Phys. Fluids* **6**, 2676–2689.

Hammond, P. S. 1983 Nonlinear adjustment of a thin annular film of viscous fluid surrounding a thread of another within a circular cylindrical pipe. *J. Fluid Mech.* **137**, 363–384.

Kalliadasis, S. & Chang, H.-C. 1994 Drop formation during coating of vertical fibres. *J. Fluid Mech.* **261**, 135–168.

Kerchman, V. I. & Frenkel, A. L. 1994 Interactions of coherent structures in a film flow – simulations of a highly nonlinear evolution equation. *Theor. Comput. Fluid Dyn.* **6**, 235–254.

Kliakhandler, I. L., Davis, S. H. & Bankoff, S. G. 2001 Viscous beads on vertical fibre. *J. Fluid Mech.* **429**, 381–390.

Papageorgiou, D. T. 1995*a* Analytical description of the breakup of liquid jets. *J. Fluid Mech.* **301**, 109–132.

Papageorgiou, D. T. 1995*b* On the breakup of viscous liquid threads. *Phys. Fluids* **7**, 1529–1544.

Quéré, D. 1990 Thin-films flowing on vertical fibers. *Europhys. Lett.* **13**, 721–726.

Quéré, D. 1999 Fluid coating on a fiber. *Annu. Rev. Fluid Mech.* **31**, 347–384.

Rayleigh, Lord 1878 On the stability of liquid jets. *Proc. Lond. Math. Soc.* **10**, 4.

Roy, R. V., Roberts, A. J. & Simpson, M. E. 2002 A lubrication model of coating flows over a curved substrate in space. *J. Fluid Mech.* **454**, 235–261.

Shen, A. Q., Gleason, B., McKinley, G. H. & Stone, H. A. 2002 Fiber coating with surfactant solutions. *Phys. Fluids* **14**, 4055–4068.

Sisoev, G. M., Matar, O. K. & Lawrence, C. J. 2003 Axisymmetric wave regimes in viscous film flow over a spinning disc. *J. Fluid Mech.* **495**, 385–411.

Tomotika, M. 1935 On the instability of a cylindrical thread of a viscous liquid surrounded by another viscous liquid. *Proc. R. Soc. Lond.* A **150**, 322–337.

https://doi.org/10.1017/S0022112006008706 Published online by Cambridge University Press